

Three-body decay of ${}^6\text{Be}$

L. V. Grigorenko^{1,2,3}, T. D. Wiser⁴, K. Mercurio⁴, R. J. Charity⁵, R. Shane⁴, L. G. Sobotka^{4,5}, J. M. Elson⁵, A. Wuosmaa⁶, A. Banu⁷, M. McCleskey⁷, L. Trache⁷, R. E. Tribble⁷, and M. V. Zhukov⁸

¹*Flerov Laboratory of Nuclear Reactions, JINR, RU-141980 Dubna, Russia.*

²*Gesellschaft für Schwerionenforschung mbH, Plankstrasse 1, D-64291, Darmstadt, Germany.*

³*RRC “The Kurchatov Institute”, Kurchatov sq. 1, 123182 Moscow, Russia.*

Departments of Physics⁴ and Chemistry⁵, Washington University, St. Louis, Missouri 63130, USA.

⁶*Department of Physics, Western Michigan University, Kalamazoo, Michigan 49008, USA.*

⁷*Cyclotron Institute, Texas A&M University, College Station, Texas 77843, USA.*

⁸*Fundamental Physics, Chalmers University of Technology, S-41296 Göteborg, Sweden.*

Three-body correlations for the ground-state decay of the lightest two-proton emitter ${}^6\text{Be}$ are studied both theoretically and experimentally. Theoretical studies are performed in a three-body hyperspherical-harmonics cluster model. In the experimental studies, the ground state of ${}^6\text{Be}$ was formed following the α decay of a ${}^{10}\text{C}$ beam inelastically excited through interactions with Be and C targets. Excellent agreement between theory and experiment is obtained demonstrating the existence of complicated correlation patterns which can elucidate the structure of ${}^6\text{Be}$ and, possibly, of the $A=6$ isobar.

PACS numbers: 23.50+z, 23.20.En, 21.60.Gx

I. INTRODUCTION

Two-proton ($2p$) radioactivity was predicted by V.I. Goldansky in 1960 [1] as an exclusively quantum-mechanical phenomenon. True three-body decay, in his terms, is a situation where the sequential emission of the particles is energetically prohibited and all the final-state fragments are emitted simultaneously. These energy conditions are illustrated for ${}^6\text{Be}$ in Fig. 1 which shows that the ${}^5\text{Li}$ ground state (g.s.) is not fully accessible for sequential decay. Since the experimental discovery of ${}^{45}\text{Fe}$ two-proton radioactivity in 2002 [3, 4], this field has made fast progress. New cases of $2p$ radioactivity were found for ${}^{54}\text{Zn}$ [6], ${}^{19}\text{Mg}$ [9], and, maybe, ${}^{48}\text{Ni}$ [5]. The $2p$ correlations were recently measured in ${}^{45}\text{Fe}$ [8], ${}^{19}\text{Mg}$ [9, 10], ${}^{16}\text{Ne}$ [10], and ${}^{10}\text{C}$ [11]. Very interesting [12], but, so far, controversial [13] case is possibility of $2p$ emission off deformed isomeric state in ${}^{94}\text{Ag}$. All these decays exhibit complex correlation patterns. It is argued that studies of these patterns could provide important information about the structure of the decaying nuclei.

With this active research as the background, there is one case which has been unduly forgotten. The ${}^6\text{Be}$ nucleus is the lightest true two-proton emitter in the sense of Goldansky. As this is expected to be the simplest case (smallest Coulomb interaction, expressed cluster structure with closed-shell core), a full understanding of its physics would provide a reliable basis for all future studies of $2p$ decay. However until now, theoretical work on ${}^6\text{Be}$ was limited to predicting the energies and widths of its states. In addition, precise experimental data do not exist. The last experimental work dedicated to correlations in ${}^6\text{Be}$ g.s. is about 20 years old.

There is one more aspect which makes the ${}^6\text{Be}$ case of special interest. In the last decade, large efforts have been directed to studies of ${}^6\text{He}$ with special emphasis to the understanding of the halo properties in this compar-

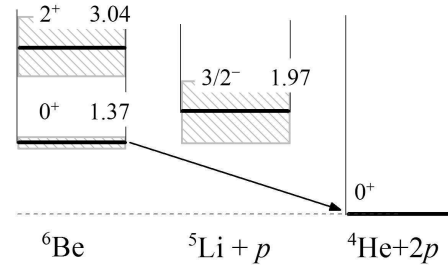


FIG. 1: Energy levels and decay scheme for ${}^6\text{Be}$ [2]. The ${}^6\text{Be}$ g.s. is a true two-proton emitter in the sense of Goldansky: the sequential decay of this state is not possible as the lowest possible intermediate, ${}^5\text{Li}$ g.s., is not energetically accessible.

atively simple and accessible case. The associated literature comprises hundreds of titles. To deduce the correlations in the neutron halo, one has to excite (e.g., Coulex) or destroy (e.g., knockout reactions) this nucleus. Therefore, the interpretation of the experimental data is influenced by the need to clarify details of the reaction mechanism [47]. However, information about mirror system can be obtained without all this “violence”. The isobaric analogue state in ${}^6\text{Be}$ decays to the $\alpha+p+p$ channel all by itself, providing the differential data on correlations. This data can be used directly to elucidate the structure of ${}^6\text{Be}$ without the need to deal with the details of the reaction mechanism. Thus an important opportunity exists for a better understanding of ${}^6\text{He}$ properties through detailed studies of the ${}^6\text{Be}$. This has not been exploited previously.

In this work, we provide detailed theoretical calculations of the three-body decay characteristics of ${}^6\text{Be}$ in a three-body cluster $\alpha+p+p$ model. We demonstrate that, in certain aspects, ${}^6\text{Be}$ may be a preferable tool for studies of the $A=6$ isobar, especially considering the high sensitivity of observables to the details of the theoretic-

cal models. We then discuss previous experimental and theoretical works on ${}^6\text{Be}$. Subsequently, we report on an experiment where ${}^6\text{Be}$ fragments are formed after the α -decay of ${}^{10}\text{C}$ projectiles excited by inelastic scattering. These data cover the complete kinematic space accessible for three-body decay and the correlations are compared to the theoretical predictions.

The $\hbar = c = 1$ system of units is used in this work. The following notations are used: E_T is the system energy and E_{3r} is the three-body resonance energy relative to the three-body $\alpha+p+p$ threshold.

II. THEORETICAL MODEL

The theoretical framework of this paper is largely the same as that developed for the two-proton radioactivity and three-body decay studies in Refs. [17, 18, 19, 20, 21, 22]. It is based on the three-body cluster model using the hyperspherical-harmonics (HH) method. The predictions obtained with this approach were found to be in very good agreement with experimental widths and momentum distributions [8, 9, 10].

In this section, we sketch the necessary formalism emphasizing only the points which differ from previous treatments.

A. Hyperspherical harmonics method

For narrow states, the time-dependent wavefunction (WF) in a finite domain can be parameterized as

$$\Psi_3^{(+)}(\rho, \Omega_\rho, t) = e^{-\frac{\Gamma}{2}t - iEt} \Psi_3^{(+)}(\rho, \Omega_\rho). \quad (1)$$

The radial part of this WF can be obtained with good precision as a solution of the inhomogeneous system of equations

$$\left(\hat{H} - E_{3r}\right) \Psi_E^{(+)}(\rho, \Omega_\rho) = -i(\Gamma/2) \Psi_{\text{box}}(\rho, \Omega_\rho), \quad (2a)$$

$$\hat{H} = \hat{T} + \hat{V}_{cp}(\mathbf{r}_{cp1}) + \hat{V}_{cp}(\mathbf{r}_{cp2}) + \hat{V}_{pp}(\mathbf{r}_{p1p2}). \quad (2b)$$

Here Ψ_{box} and E_{3r} are the eigenfunction and the eigenvalue of the equation

$$\left(\hat{H} - E\right) \Psi_{\text{box}}(\rho, \Omega_\rho) = 0, \quad (3)$$

solved with a ‘‘box’’ boundary condition at large ρ . The hyperspherical coordinates are defined via the Jacobi vectors

$$\mathbf{X} = \mathbf{r}_{p1} - \mathbf{r}_{p2}, \quad \mathbf{Y} = (\mathbf{r}_{p1} + \mathbf{r}_{p2})/2 - \mathbf{r}_c, \quad (4a)$$

$$\rho^2 = \frac{2}{3}(r_{cp1}^2 + r_{cp2}^2) + \frac{1}{6}r_{p1p2}^2 = \frac{1}{2}X^2 + \frac{4}{3}Y^2, \quad (4b)$$

$$\Omega_\rho = \{\theta_\rho, \Omega_x, \Omega_y\}, \quad \theta_\rho = \arctan\left[\sqrt{\frac{3}{8}}\frac{X}{Y}\right]. \quad (4c)$$

These Jacobi variables are given in ‘‘T’’ Jacobi system (see Fig. 2). The hyperradial components $\chi_{K\gamma}^{(+)}(\rho)$ of the WF equation 2, possessing the pure outgoing asymptotics

$$\Psi_E^{(+)}(\rho, \Omega_\rho) = \rho^{-5/2} \sum_{K\gamma}^{K_{\max}} \chi_{K\gamma}^{(+)}(\varkappa\rho) \mathcal{J}_{K\gamma}^{JM}(\Omega_\rho), \quad (5)$$

are matched to approximate boundary conditions of the three-body Coulomb problem obtained in Ref. [16]. The radial components of this WF at large ρ values can be represented as

$$\chi_{K\gamma}^{(+)}(\varkappa\rho) \sim A_{K L l_x l_y}^{JSSx}(\varkappa) \tilde{\mathcal{H}}_{K\gamma}^{(+)}(\varkappa\rho). \quad (6)$$

In general, the functions $\tilde{\mathcal{H}}_{K\gamma}^{(+)}$ are some linear combinations of Coulomb functions with the outgoing asymptotic $G + iF$. The functions $\mathcal{J}_{K\gamma}^{JM}(\Omega_\rho)$ are hyperspherical harmonics coupled with spin functions to total spin J . ‘‘Multyindex’’ γ denote the complete set of quantum numbers except the principal quantum number K : $\gamma = \{L, S, l_x, l_y\}$. The value K_{\max} truncates the hyperspherical expansion. The hypermoment \varkappa is expressed via the energies of the subsystems E_x, E_y or via the Jacobi momenta k_x, k_y conjugate to Jacobi coordinates X, Y :

$$\mathbf{k}_x = \frac{1}{2}(\mathbf{k}_{p1} - \mathbf{k}_{p2}), \quad (7a)$$

$$\mathbf{k}_y = \frac{2}{3}(\mathbf{k}_{p1} + \mathbf{k}_{p2}) - \frac{1}{3}\mathbf{k}_c, \quad (7b)$$

$$\varkappa^2 = 2ME_T = 2M(E_x + E_y) = 2k_x^2 + \frac{3}{4}k_y^2, \quad (7c)$$

$$\Omega_\varkappa = \{\theta_k, \Omega_{k_x}, \Omega_{k_y}\}, \quad \theta_k = \arctan[E_x/E_y]. \quad (7d)$$

A more detailed picture of the ‘‘T’’ and ‘‘Y’’ Jacobi systems in coordinate and momentum spaces can be found in Fig. 2.

The set of coupled equations for the functions $\chi^{(+)}$ has the form

$$\left[\frac{d^2}{d\rho^2} - \frac{\mathcal{L}(\mathcal{L}+1)}{\rho^2} + 2M\{E - V_{K\gamma, K'\gamma'}(\rho)\}\right] \chi_{K\gamma}^{(+)}(\rho) = 2M \sum_{K'\gamma'} V_{K\gamma, K'\gamma'}(\rho) \chi_{K'\gamma'}^{(+)}(\rho) + i\Gamma M \chi_{K\gamma}(\rho), \quad (8)$$

where $\mathcal{L} = K + 3/2$ is ‘‘effective angular momentum’’ and $V_{K\gamma, K'\gamma'}(\rho)$ is ‘‘three-body potential’’ (matrix elements of the pairwise potentials);

$$V_{K\gamma, K'\gamma'}(\rho) = \int d\Omega_\rho \mathcal{J}_{K'\gamma'}^{JM*}(\Omega_\rho) \sum_{i < j} V_{ij}(\mathbf{r}_{ij}) \mathcal{J}_{K\gamma}^{JM}(\Omega_\rho) \quad (9)$$

and

$$\Psi_{\text{box}}(\rho, \Omega_\rho) = \rho^{-5/2} \sum_{K\gamma} \chi_{K\gamma}(\rho) \mathcal{J}_{K\gamma}^{JM}(\Omega_\rho). \quad (10)$$

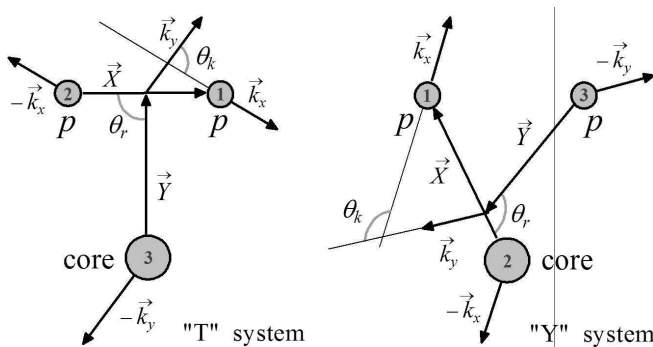


FIG. 2: Independent “T” and “Y” Jacobi systems for the core+ $N+N$ three-body system in coordinate and momentum spaces.

B. Width and momentum distribution

Equation 2 is first solved with an arbitrary value of Γ and then the width is found according to the “natural” definition as the flux j through a hypersphere with large radius ρ_{\max} divided by the internal normalization N (“number of particles” inside the sphere):

$$\Gamma_{\text{nat}} = j/N, \quad (11)$$

$$j = \int d\Omega_\rho \frac{dj(\rho_{\max}, \Omega_\rho)}{d\Omega_\rho}, \quad (12)$$

$$N = \sum_{K\gamma} N_{K\gamma} = \sum_{K\gamma} \int_0^{\rho_{\text{int}}} d\rho \left| \chi_{K\gamma}^{(+)}(\rho) \right|^2. \quad (13)$$

The differential flux through the hypersphere ρ_{\max} is defined as

$$\frac{dj(\rho_{\max}, \Omega_\rho)}{d\Omega_\rho} = \text{Im} \left[\Psi_3^{(+)\dagger} \rho^{5/2} \frac{d}{M d\rho} \rho^{5/2} \Psi_3^{(+)} \right] \Big|_{\rho=\rho_{\max}}. \quad (14)$$

If, for sufficiently large ρ , the coefficients $A_{LL_x L_y}^{KSS_x}$ in Eq. 6 become independent of ρ , then the coordinate distribution becomes identical to the momentum distribution, i.e.,

$$\frac{j(\rho_{\max}, \Omega_\rho)}{d\Omega_\rho} \rightarrow \frac{dj(\Omega_\varkappa)}{d\Omega_\varkappa}. \quad (15)$$

Further discussions of the validity of this approximation (Eq. 15), and detailed expressions for the momentum distributions, can be found in Ref. [16].

C. Potentials

The NN potential is taken either as a simple s -wave single-Gaussian form BJ (from the book of Brown and Jackson [24])

$$V(r) = V_0 \exp(-r^2/r_0^2), \quad (16)$$

with $V_0 = -31$ MeV and $r_0 = 1.8$ fm, or the realistic “soft-core” potential GPT (Gogny-Pires-de Tourreil [25]).

The Coulomb potential of the homogeneously charged sphere $r_{\text{sph}} = 1.852$ fm is used in the α - p channel. In addition for this channel, we use an ℓ -dependent potential SBB (Sack-Biedenharn-Breit [23])

$$V(r) = V_c^{(\ell)} \exp(-r^2/r_0^2) + (\ell \cdot \mathbf{s}) V_{\ell s} \exp(-r^2/r_0^2), \quad (17)$$

where $r_0 = 2.30$ fm, $V_c^{(0)} = 50$ MeV, $V_c^{(1)} = -47.32$ MeV, $V_c^{(2)} = -23$ MeV, and $V_{\ell s} = -11.71$ MeV. Historically, a somewhat modified SBBM potential has been used in the calculations of $A=6$ isobars in order to better reproduce the binding energies (e.g., Ref. [26]). Later it was realized that it is more consistent to provide the phenomenological binding-energy correction using an additional short-range three-body potential (see, e.g., the discussion in Ref. [21]). In this work, we used a short-range three-body potential of the form

$$V_3(\rho) = \delta_{K\gamma, K'\gamma'} V_3^{(0)} / [1 + \exp((\rho - \rho_0)/d_3)], \quad (18)$$

where $\rho_0 = 2.5$ fm and $d_3 = 0.4$ fm. This “short-range” three-body potential (note the small diffuseness) does not distort the interactions in the subbarrier region which was found to be important for consistent studies of decay properties.

Three sets of nuclear potential are employed in this work. They are denoted as P1 (SBB+BJ), P2 (SBB+GPT), and P3 (SBBM+GPT). The values of $V_3^{(0)}$ used with potential sets P1, P2, and P3 are -11.14 MeV, -13.22 MeV, and -0.64 MeV, respectively. Throughout this paper when the potential set is not specified, the results of the calculations with the P2 set are shown.

D. Reaction models

In general, different definitions for the width of a decaying state coincide only in the limit when the width is very small. For the ground state of ${}^6\text{Be}$, the definition of Eq. 11 is not very precise, as this state is comparatively broad ($\Gamma = 92 \pm 6$ keV) and thus the internal normalization N (Eq. 13) is sensitive to the integration limit ρ_{int} . For reasonable values of ρ_{int} ranging from 10 – 20 fm, the uncertainty in the width (Γ_{nat}) is about 25% [see Sec. III C, Fig. 12(a)]. This problem does not exist for narrow $2p$ emitters ($\Gamma < 1$ eV) where the WFs $\chi_{K\gamma}^{(+)}$ are vanishingly small under the Coulomb barrier. The densities for the dominating components of the ${}^6\text{He}$ and ${}^6\text{Be}$ WFs are shown in Fig. 3. For ${}^6\text{Be}$, it is clear that the WF under the barrier is not negligible.

For moderately broad states, there are alternative ways to derive the width. These involve either the study of the $3 \rightarrow 3$ scattering or the study of a particular reaction. For technical reasons, the latter is preferable for our application. For example, in order to determine the population

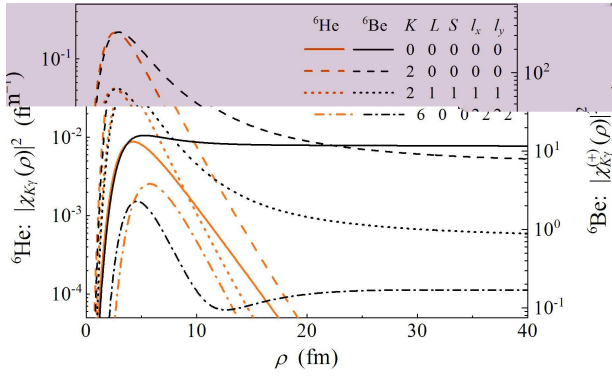


FIG. 3: Densities $|\chi_{K\gamma}(\rho)|^2$ and $|\chi_{K\gamma}^{(+)}(\rho)|^2$ for the largest components of the ${}^6\text{He}$ and ${}^6\text{Be}$ g.s. WFs.

of ${}^6\text{Be}$ in a charge-exchange reaction on ${}^6\text{Li}$ at zero angle, Eq. 2 can be reformulated as

$$(\hat{H} - E_T) \Psi_{6\text{Be}}^{(+)}(\rho, \Omega_\rho) = \sum_i \tau_i^- \sum_M \sigma_i^{(M)} \Psi_{6\text{Li}}^{JM}(\rho, \Omega_\rho). \quad (19)$$

This notation is based on the fact that for angles close to zero, the transitions in charge-exchange reactions, in the limit of high energies, are provided by the Gamow-Teller operator. Although this reaction is different to the one studied experimentally in this work, it is sufficient for our computational purposes. Namely, we will demonstrate that for the ${}^6\text{Be}$ g.s. population, the choice of the reaction mechanism is not very important (there are still some exclusive situations, which we will discuss elsewhere).

Using the source function of Eq. 19, the cross section for the population of the three-body continuum is proportional to the outgoing flux of the three particles on a hypersphere of some large radius $\rho = \rho_{\text{max}}$:

$$d\sigma(E_T)/dE_T \sim j(\rho_{\text{max}}, \Omega_\rho). \quad (20)$$

Differentials of this flux on the hypersphere provide angular and energy distributions among the decay products at the given decay energy E_T in analogy with Eqs. 14 and 15.

E. “Feshbach” reduction

Although the HH calculations for ${}^6\text{Be}$ can be performed with $K_{\text{max}} = 22 - 26$, these basis sizes may not be sufficient to obtain good convergence for all observables. However, the basis size can be effectively increased using the adiabatic procedure based on the so-called Feshbach reduction (FR) [21]. Feshbach reduction eliminates from the total WF $\Psi = \Psi_p + \Psi_q$, an arbitrary subspace q using the Green’s function of this subspace:

$$H_p = T_p + V_p - V_{pq} G_q V_{pq}. \quad (21)$$

In an adiabatic approximation, we can assume that the radial part of kinetic energy is small under the centrifugal barrier in the channels where this barrier is large and can be approximated as a constant. In this approximation, the FR procedure is reduced to the construction of effective three-body interactions $V_{K\gamma, K'\gamma'}^{\text{eff}}$ by the matrix operations

$$G_{K\gamma, K'\gamma'}^{-1} = (H - E)_{K\gamma, K'\gamma'} = V_{K\gamma, K'\gamma'} + \left[E_f - E + \frac{(K + 3/2)(K + 5/2)}{2M\rho^2} \right] \delta_{K\gamma, K'\gamma'} \quad (22)$$

where

$$V_{K\gamma, K'\gamma'}^{\text{eff}} = V_{K\gamma, K'\gamma'} - \sum_{\bar{K}\bar{\gamma}} V_{K\gamma, \bar{K}\bar{\gamma}} G_{\bar{K}\bar{\gamma}, \bar{K}\bar{\gamma}} V_{\bar{K}\bar{\gamma}, K'\gamma'}. \quad (23)$$

Summations over indexes with the bar are made for the eliminated channels. We typically eliminate the channels with $K > K_{FR}$, where K_{FR} provides the sector of the hyperspherical basis where the calculations remains fully dynamical. We take the “Feshbach energy” E_f in our calculations as $E_f \equiv E$.

There are two ways to control the reliability of the FR procedure. (i) The “soft” method is to vary K_{FR} from the maximum attainable in the dynamic calculations downwards for fixed K_{max} . The results, in principle, should coincide. (ii) The “safe” method is to take K_{max} in the range attainable for dynamic calculations and compare the “reduced” $K_{\text{max}} \rightarrow K_{FR}$ calculations (with much smaller dynamic basis size K_{FR}) with completely dynamic calculations with K_{max} . For ${}^6\text{Be}$, these considerations show that we can safely use $K_{FR} = 14$. However, the even safer value of $K_{FR} = 22$ is used in this work.

III. GROUND STATE

There are several convergence characteristics that should be understood before reliable results on ${}^6\text{Be}$ are obtained. The convergence character is quite different for all the observables of interest and also depend strongly on the interaction in the p - p channel.

A. Convergence of energy and width

Because of the problem mentioned in Sect. IID, we need to begin our studies with the energy dependence of the cross section. The convergence of the cross-section profile with increasing size of the basis is demonstrated in Fig. 4. The main character of the convergence is clearly seen here; the centroid energy decreases, while the width grows significantly.

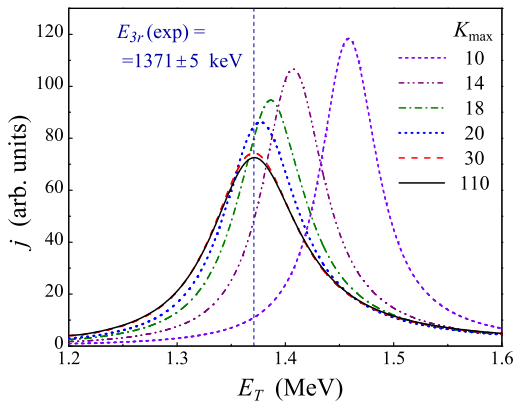


FIG. 4: (Color online) Energy profile of the ${}^6\text{Be}$ g.s. populated in the charge-exchange reaction with ${}^6\text{Li}$. The results are shown as a function of the basis size K_{max} where $K_{FR} = 22$. For $K_{\text{max}} \leq K_{FR}$ and no Feshbach reduction is needed.

The cross section for the ${}^6\text{Be}$ g.s. population, shown in Fig. 4, clearly has a profile close to a slightly asymmetric Lorentzian. Can the profile of this three-body resonance be described by appropriately-modified R-matrix type expressions? A curious result is obtained here, the resonance profile, shown in Fig. 4 by the solid curve, can be fit with amazing precision by the following expression:

$$\sigma(E_T) \sim \frac{\Gamma(E_T)}{(E_T - E_{3r})^2 + \Gamma(E_T)^2/4}, \quad (24)$$

$$\Gamma(E_T) = \Gamma_0 \left[\alpha \left(\frac{E_T}{E_{3r}} \right)^2 + (1 - \alpha) \left(\frac{E_T}{E_{3r}} \right)^4 \right], \quad (25)$$

where $\Gamma_0 = 98$ keV and $\alpha = 0.65$. Equation 24 is the ordinary expression for the inelastic cross section of an isolated resonance. The parameterization of Eq. 25 was chosen because, for the single-channel penetration through the hyperspherical barrier with $K = 0$, the energy dependence of the width can be inferred as $\Gamma(E_T) \sim E_T^2$. For $K = 2$ one has $\Gamma(E_T) \sim E_T^4$ (see, e.g., Ref. [27]). It should be understood that the $K = 0$ component is equivalent to a “phase volume” with the characteristic energy behavior of $\sim E^2$. The energy dependence of the width obtained by Eq. 25 almost coincides with the calculated dependence of this width in a reasonable energy range (see Fig. 5 when one uses $\alpha=0.63$ and 0.52 for potential P2 and P3, respectively). If we take the actual calculated partial widths for the $K = 0$ and 2 components from Table V, then the value of α can be estimated as

$$\alpha = N_{K=0}/(N_{K=0} + N_{K=2}) \approx 0.58. \quad (26)$$

This is quite close to the value 0.65 obtained by a fit.

The existence of this simple approximation, despite the fact that there are Coulomb interactions and other numerous channels involved, may demonstrate that the dynamics of the ${}^6\text{Be}$ g.s. decay is largely defined by the

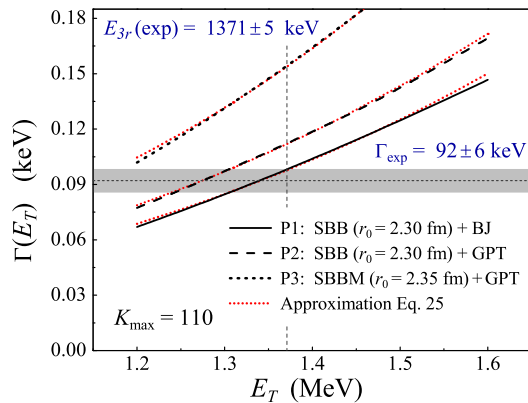


FIG. 5: (Color online) Dependence of ${}^6\text{Be}$ g.s. width on the decay energy E_T . Predictions are shown for the three potential set P1-P3. The dotted curves show the approximation of Eq. 25.

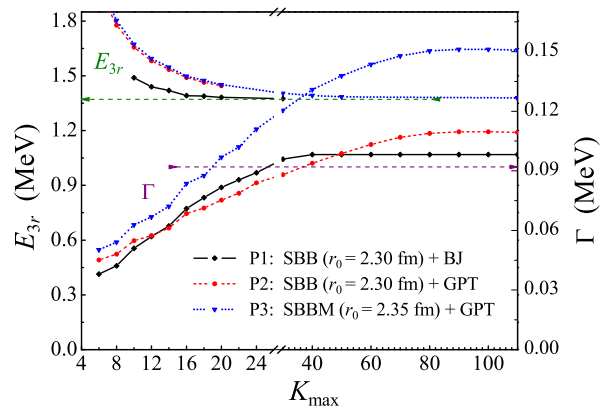


FIG. 6: (Color online) Convergence of the resonance energy E_{3r} and the width Γ for the ${}^6\text{Be}$ g.s. as a function of the basis size K_{max} .

penetration through the hyperspherical barriers. Possibly, this is due to the comparatively large ${}^6\text{Be}$ decay energy of $E_{3r} = 1.371$ MeV. Simple estimates shows that the state is “sitting” somewhere straight on the top of the Coulomb barrier.

It was found that the value of $j(E_T)$ for ${}^6\text{Be}$ g.s. is not sensitive to the particular choice of the source in Eq. 19, which is typically within the width of the line [48]. This means that the width defined by the procedure of Eqs. 24 and 25 is very reliable. We can fine tune the value ρ_{int} in Eq. 13 so that the definition of the width in Eq. 11 coincides with the definition in Eq. 24 and subsequently we can reliably use Eq. 11. All of the potential sets P1-P3 needed $\rho_{\text{int}} \approx 12.5$ fm.

The convergences of the predicted resonance energy and width as a function of the hyperspherical basis size are shown in Fig. 6 for each of the potential sets. In all cases, our calculations are fully converged. The resonance energies are forced to approach the experimental

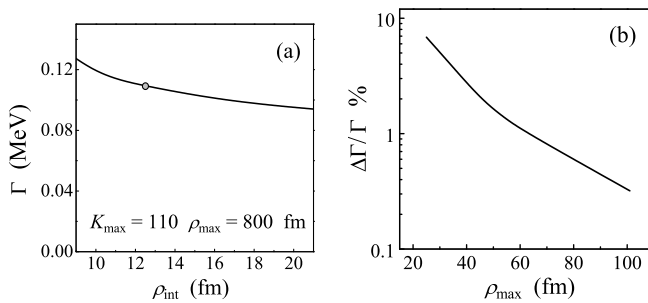


FIG. 7: (a) Sensitivity of the width as defined in Eq. 11 to the size of the “internal region” ρ_{int} . The dot shows the value of ρ_{int} at which this width coincides with that defined by the cross-section profile Eqs. 19, 20, 24, and 25. (b) Relative precision of the width as a function of the matching radius ρ_{max} .

value $E_{3r} = 1.371$ MeV. This is achieved by fine tuning the phenomenological potential of Eq. 18; this is a necessary approach in order to provide reasonable predictions for the decay characteristics. We can see that while the calculations with P1 and P2 (SBB potential in the α - p channel) are in good agreement with each other and with the experimental value, the width obtained with P3 (SBBM potential) is far too large.

An expected feature observed here is the much slower convergence of the calculations with a realistic potential in the NN channel. An important, but often disregarded fact, which one can see in Fig. 6, is the much slower convergence of the width as compared to the energy. This means that, *in general, an energy convergence does not guarantee the convergence of other important characteristics*. As we will see in Sect. III C, the situation with momentum distributions is even more complicated than it is for the widths.

The sensitivity of the width to a number of the other parameters in the calculations is demonstrated in Fig. 7. Figure 7(a) shows the sensitivity of the width defined by Eq. 11 to the size ρ_{int} of the region where the internal normalization is calculated. The stability of the calculations to the dynamical range ρ_{max} is demonstrated in Fig. 7(b). To attain 1% numerical precision in the width calculations, we need to go beyond 60 fm in the hyperradius ρ .

B. Features of the momentum distributions in ${}^6\text{Be}$

The correlations in the decay of ${}^6\text{Be}$ include both the generic features of the $2p$ decays, as discussed earlier in Refs. [16, 20, 21], and some peculiarities which we present in more detail now. For nuclear states with $J \leq 1/2$ (as is the case for ${}^6\text{Be}$ g.s. decay), the three-body correlations can be completely described by 2 parameters. There are a total of 9 degrees of freedom for three particles in the final state. Of these, three describe the center-of-mass motion, three describe the Euler rotation of the decay plane (for

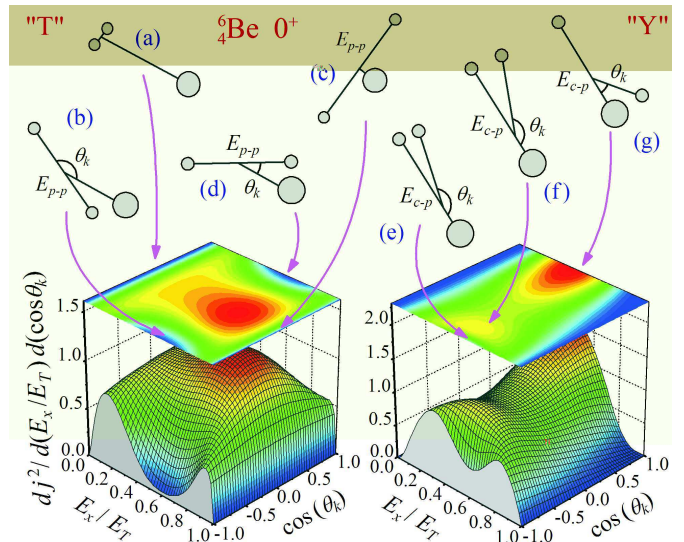


FIG. 8: (Color online) Complete correlation picture for ${}^6\text{Be}$ g.s. decay, presented in “T” and “Y” Jacobi systems.

$J \leq 1$ all its orientations are quantum-mechanically identical), and the three-body decay energy is fixed. Thus we are left with two parameters to describe the correlations. It is convenient to choose the energy distribution parameter ε between any two of the particles and the angle θ_k between the Jacobi momenta:

$$\varepsilon = E_x / E_T \quad , \quad \cos(\theta_k) = \frac{\mathbf{k}_x \cdot \mathbf{k}_y}{k_x k_y}. \quad (27)$$

These parameters can be constructed in any Jacobi system and for ${}^6\text{Be}$ there are two “irreducible” Jacobi systems, called “T” and “Y”, see Fig. 2. The distributions constructed in different Jacobi systems are just different representations of the same physical picture. However, different aspects of the correlations may be better revealed in a particular Jacobi system.

Predictions for the complete correlation picture of ${}^6\text{Be}$ g.s. decay are shown in Fig. 8 for both the “T” and “Y” Jacobi systems. Schematic figures are included in this figure to help in visualizing the correlations associated with different regions of the Jacobi plots. The main features of these distributions are:

1. The energy distribution in the “T” system has a double-humped profile which is an indication of the $[p^2]$ configuration dominance which was pointed out in very early papers on ${}^6\text{Be}$ [28, 29, 30]. This double-humped configuration is expressed more in coordinate space (see the internal region in Fig. 13) and only marginally “survives” in the asymptotic region. The internal peaks in Fig. 13 have the special names of “diproton” (protons are close to each other) and “cigar” (protons are in-line with α -particle) configurations [26].
2. There are kinematical regions where the presence of

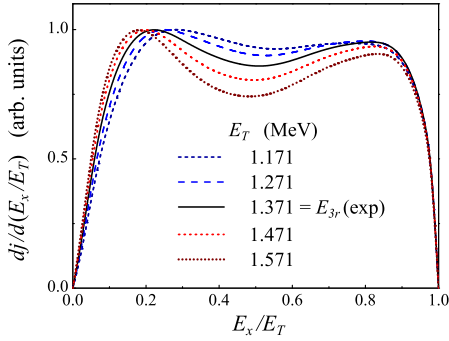


FIG. 9: (Color online) Dependence of energy distribution between the proton (“T” system) in the decay of ${}^6\text{Be}$ g.s. on the decay energy E_T .

particles is suppressed due to Coulomb repulsions. Strong suppression in the α - p channel in regions (b) and (d) and a smaller suppression in the p - p channel in region (e) are predicted.

- There are enhancements due to the p - p final-state interaction in regions (a) and (f). The ${}^5\text{Li}$ g.s. resonance in the α - p channel is not accessible for decay. However, some hint of its presence can be obtained from the enhancement in region (g). This is a “back-to-back” configuration, where protons fly in the opposite directions. However, the reason for the enhancement of such a configuration is not fully understood.
- The angular dependence in the “T” system almost vanishes for regions (a) and (c) ($E_x/E_T \sim 0$ and $E_x/E_T \sim 1$). It is clear that in the limit $E_x/E_T \rightarrow 0$ and $E_x/E_T \rightarrow 1$ the dependence on the relative orientation of \mathbf{k}_x and \mathbf{k}_y should become degenerate. However at intermediate values of E_x/E_T , this dependence is very pronounced.
- The total-energy distribution in the “Y” system (see Fig. 10 for the projected distributions) is almost a symmetric bell-shape. This is the energy distribution between the core and one of the protons and its symmetry reflects the symmetry between protons. In heavy two-proton emitters, this distribution becomes very narrow and almost completely symmetric.

The correlation predictions shown in Fig. 8 are obtained on resonance. The dependence of energy correlation on the decay energy of ${}^6\text{Be}$ is demonstrated in Fig. 9. The double-humped shape of this spectrum becomes less pronounced when the energy decreases. With smaller energy, the relative contribution of the $[s^2]$ configuration to the decay grows compared to the $[p^2]$ configuration. The latter has an additional centrifugal component to the barrier and its contribution to the width

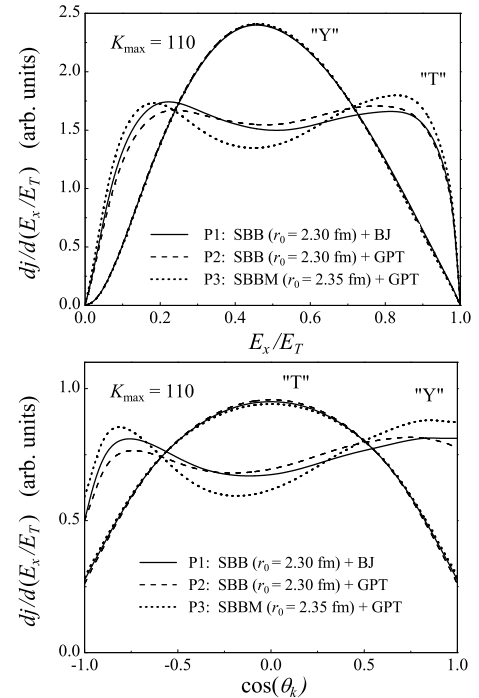


FIG. 10: Sensitivity of the energy and angular distributions in the decay of ${}^6\text{Be}$ g.s. to the choice of the potential set. Results are shown for both the “T” and “Y” Jacobi systems.

should be suppressed at low energies. The pure $[s^2]$ configuration should produce a featureless “phase-volume” energy distribution

$$dj/dE_x \sim \sqrt{E_x(E_T - E_x)}. \quad (28)$$

The sensitivity of the projected distributions to the choice of the potential set P1-P3 is demonstrated in Fig. 10. The angular distribution in the “T” system and the energy distribution in “Y” systems are practically insensitive to this choice. The other projected distributions demonstrate sensitivity on the level of 10 – 15%. However, local differences in certain kinematical regions are much larger.

Figures 8 and 10 demonstrate what we call the “softness” of the ${}^6\text{Be}$ system: minor variations in the conditions or computational details lead to a noticeable variations in the observable properties. Heavier $2p$ emitters appear to be much “stiffer” in this respect.

C. Convergence of the momentum distributions

In our calculations there are two projected distributions which are practically insensitive to convergence issues (the angular distribution in the “T” system and the energy distribution in the “Y” system). The other two distributions (the angular distribution in the “Y” system and the energy distribution in the “T” system) demonstrate strong sensitivity. The convergence of the energy

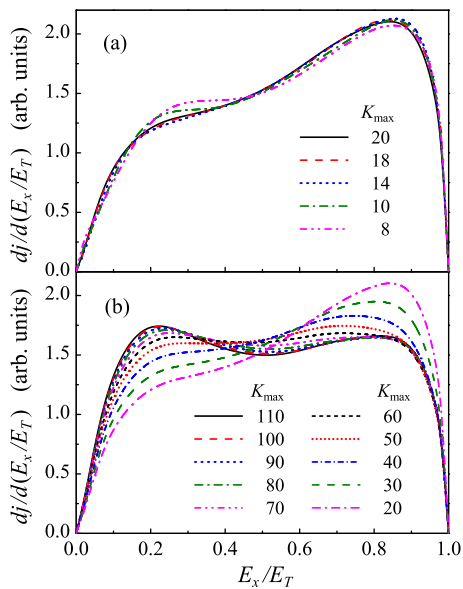


FIG. 11: (Color online) Convergence of the “T” energy distribution in the decay of ${}^6\text{Be}$ g.s. as a function of the basis size K_{max} .

distributions are illustrated in Figs. 11 and 12.

The convergence of the energy distribution between protons has a very curious character, see Fig. 11. From $K_{\text{max}} = 8$ to $K_{\text{max}} = 22$ this distribution is very stable [several curves almost coincide, see Fig. 9(a)]. Then from $K_{\text{max}} = 24$ to $K_{\text{max}} \sim 70$ the distribution changes qualitatively, and up to $K_{\text{max}} \sim 100$ there is still a noticeable variation [Fig. 9(b)]. Hopefully with $K_{\text{max}} = 110$, we have a well converged distribution. Calculations with small basis sizes (e.g., $K_{\text{max}} \leq 70$) for ${}^6\text{Be}$ should provide a qualitatively wrong energy distribution in the “T” system. Similarly for the angular distribution in the “Y” system.

This “softness” of the ${}^6\text{Be}$ system makes it a very complicated object to study. Minimum basis sizes which provide convergence for the energy and width are far from sufficient for calculations of momentum distributions. This is a feature which we probably do not face in heavier $2p$ emitters as the Coulomb interaction in the core- p channel plays a more dominant role in the decay dynamics.

The radial convergence of the energy distributions is illustrated in Fig. 12. Calculations with $\rho_{\text{max}} < 300$ fm are clearly insufficient to stabilize the distribution. However by $\rho_{\text{max}} = 800$ fm, the distributions seem to be well converged. Could there be some noticeable modifications of the distributions due to further propagation in the long-range Coulomb field? This question was analyzed in Ref. [16] for ${}^{45}\text{Fe}$ using the classical trajectory approach. The complete stabilization takes place in ${}^{45}\text{Fe}$ at $\rho \sim (3 - 6) \times 10^4$ fm, with a major part of the effect originating at $\rho \lesssim 1 \times 10^4$ fm. The decay energies of ${}^6\text{Be}$ and ${}^{45}\text{Fe}$ g.s. are similar and the Coulomb interaction is

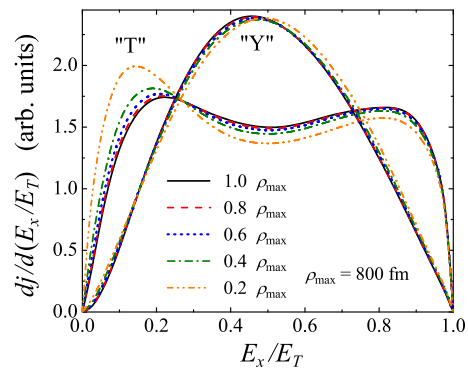


FIG. 12: (Color online) Dependence of energy distribution in the decay of ${}^6\text{Be}$ g.s. on the maximal dynamic range of the calculation ρ_{max} . For the “T” Jacobi system, E_x is energy between two protons and in the “Y” Jacobi system, E_x is energy between core and one of the protons.

~ 12 times weaker in ${}^6\text{Be}$. Therefore, the majority of the long-range effects should be taken into account in calculations with $\rho_{\text{max}} \sim 1000$ fm. The ${}^6\text{Be}$ calculations of this work were typically done with $\rho_{\text{max}} = 1200$ fm.

D. Structure of the ${}^6\text{He}$ and ${}^6\text{Be}$ g.s.

From another point of view, one can benefit from the “softness” of ${}^6\text{Be}$ system. The high sensitivity of the observables to the details of the model ingredients increase our ability to discriminate these features and hence improve our ability to elucidate the details of the nuclear structure.

Detailed information about the ${}^6\text{He}$ and ${}^6\text{Be}$ g.s. WFs is provided in Table V. In general, there is high degree of isobaric symmetry between the ${}^6\text{He}$ and ${}^6\text{Be}$ WFs in the internal region. This is not true, however, for the $K = 0$ component, which differs the most. The reason for this is shown in Fig. 3 where the magnitude of the $K = 0$ WF in asymptotic region is comparable to its magnitude in the nuclear interior. Hence the nuclear boundary is not defined for this component in ${}^6\text{Be}$. This is also seen in Table I, which provides the information about the WF

TABLE I: Weights of the shell-model-like configurations [l^2] in the ${}^6\text{He}$ and ${}^6\text{Be}$ g.s. WFs in percent for the Jacobi “Y” system. The normalizations of the ${}^6\text{Be}$ components are found for integration radius $\rho_{\text{int}} = 12.5$ fm.

	${}^6\text{He}$			${}^6\text{Be}$		
[l^2]	P1	P2	P3	P1	P2	P3
[s^2]	8.11	8.58	8.35	10.54	11.15	10.84
[p^2]	90.91	90.30	90.37	87.98	87.18	87.17
[d^2]	0.47	0.53	0.61	0.69	0.77	0.95
[f^2]	0.41	0.43	0.50	0.60	0.65	0.77

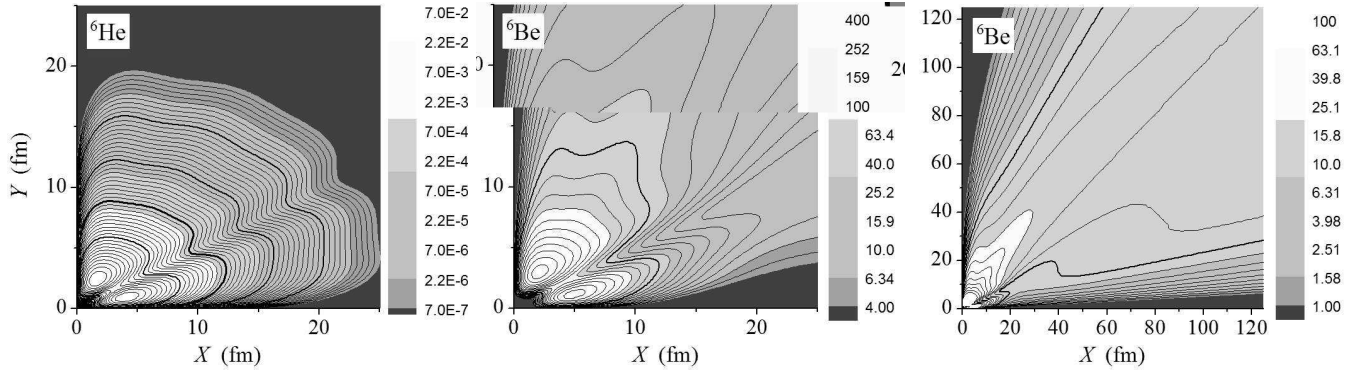


FIG. 13: Spatial correlation densities $|\Psi(X, Y)|^2$ for the ${}^6\text{He}$ and ${}^6\text{Be}$ g.s. WFs in the ‘‘T’’ system. For ${}^6\text{Be}$, two panels provide the view in different radial ranges. Pay attention to difference in the scales. The variation from the top to the thick contour line in the ${}^6\text{He}$ panel corresponds to the whole scale variation in the two ${}^6\text{Be}$ panels.

in approximate ‘‘shell model’’ terms. After looking at the radial behavior of the WF’s components in Fig. 3, we find that the concept of isobaric symmetry is relevant here strictly speaking *only* for the most interior region of the WF ($\rho < 4 - 5$ fm). Beyond this point the radial behavior in ${}^6\text{He}$ and ${}^6\text{Be}$ differ drastically.

The weights of the components in Tables V and I are in *very* good relative agreement for the different potential sets P1-P3. Evidently these major features of the structure are not that sensitive to the fine details of the interactions.

It can be seen that the partial widths Γ_i of the ${}^6\text{Be}$ WF components in Table V are drastically different as compared to weights N_i in the internal region. This is a reflection of complicated dynamics in $2p$ decays, the WFs are strongly ‘‘rearranged’’ in the subbarrier region and by

the long-range Coulomb pairwise fields. The ${}^6\text{He}$ and ${}^6\text{Be}$ WF correlation densities are shown in Fig. 13. The WFs are nearly identical in the internal region, while in the asymptotic region for ${}^6\text{Be}$ we can clearly see how this ‘‘rearrangement’’ is taking place. Comparing different potential sets P1-P3 in Table V, we see that P1 and P2 calculations are almost identical, while the major partial width in P3 differs strongly. We conclude that the decay dynamics is mainly defined by core- p interaction.

Geometric properties of the ${}^6\text{He}$ g.s. WF and several observables obtained for ${}^6\text{He}$ and ${}^6\text{Be}$ g.s. are shown in Table II. The root mean square values are given for ρ , r_{NN} (distance between valence nucleons), r_{cN} (distance between nucleon and core), r_N (distance between valence nucleon and c.m.), r_{cN} (distance between core and c.m.). The differences between these geometric characteristics for P1 and P2 are typically around 1%. In the case of P3, the differences are significantly larger. The B_{GT} values obtained with P1-P3 also agree within 1.5%, but all differ more from the experimental value. Here, the ‘‘experimental’’ B_{GT} value is obtained using the ${}^6\text{He}$ lifetime $\tau_{1/2} = 806.7 \pm 1.5$ ms [2], and the β -decay constants of $ft(0^+ \rightarrow 0^+) = 3072.40$ s and $\lambda = 1.268$. It has already been discussed in the literature that the 4 – 7% disagreement here could be connected with both the WF quality and the renormalization of the weak constant [26]. Therefore, we give no definite conclusion about quality of the models here.

The next most precisely known characteristic for ${}^6\text{He}$ is its charge radius. Recent studies have defined r_{ch} with increasing precision [33, 34]. The relative uncertainty of this value is now about 0.5%, while variations in the calculated value are around 4% for P1-P3. However, comparison of this value with those theoretically calculated is not completely model independent. The theoretically calculated charge radius of ${}^6\text{He}$ is noticeably sensitive to the neutron charge radius. The latter is inferred theoretically, rather than measured experimentally. This means that there exists considerable systematic uncertainty in the determination of the charge radii. According to our

TABLE II: Radial properties of the ${}^6\text{He}$ g.s. WF and some observables obtained for ${}^6\text{He}$ and ${}^6\text{Be}$ g.s. with potentials P1, P2, P3.

value	P1	P2	P3	Exp.
$\langle \rho \rangle$ (fm)	5.088	5.156	5.491	
$\langle r_{NN} \rangle$ (fm)	4.482	4.502	4.884	
$\langle r_{cN} \rangle$ (fm)	4.113	4.172	4.430	
$\langle r_N \rangle$ (fm)	3.211	3.248	3.469	
$\langle r_c \rangle$ (fm)	1.321	1.171	1.232	
r_{mat} (fm)	2.396	2.421	2.540	2.30 ± 0.07 [35] 2.48 ± 0.03 [36]
r_{ch}^a (fm)	2.103	2.012	2.048	2.054 ± 0.014 [33]
r_{ch}^b (fm)	2.113	2.043	2.079	2.068 ± 0.011 [34]
$B_{GT}({}^6\text{He} \rightarrow {}^6\text{Li})$	5.004	5.058	4.930	4.745 ± 0.009 [2]
ΔE_{coul} (MeV)	2.351	2.302	2.111	2.344 [2]
$\Gamma({}^6\text{Be}_{\text{g.s.}})$ (keV)	98	112	154	92 ± 6 [2]

^aTheoretical values in this row are obtained using the generally accepted value for the neutron charge radius $r_{\text{ch}}^2(n) = -0.1161$ fm².

^bTheoretical values in this row are obtained using $r_{\text{ch}}^2(n) = 0.012$ fm² [34].

estimates, this uncertainty can be as large as 2%. This fact somewhat relieves the constraints on the WF connected with this observable. One can see in Table II that the P2 and P3 calculations, containing realistic NN potentials can be regarded as consistent with the experiment.

The matter radius of ${}^6\text{He}$ is defined in the cluster model using the matter radius of the α -particle. The value $r_{\text{mat}}(\alpha) = 1.464$ fm is derived from the charge radius $r_{\text{ch}}(\alpha) = 1.671$ using the neutron and proton charge radii; $r_{\text{ch}}^2(n) = -0.1161$ fm², $r_{\text{ch}}(p) = 0.875$ fm. The experimental data on matter radii have large a systematic uncertainty. This is probably the reason for the controversial signal obtained in different experiments (see two examples in Table II). This observable so far does not seem to have discriminative power for theoretical models.

The Coulomb shift ΔE_{Coul} and ${}^6\text{Be}$ g.s. width obtained with P1 and P2 are in a good agreement with experiment. Some overestimation of the width in the three-body cluster model can be expected due to the admixture of different configurations in ${}^6\text{Be}$ WF. The weight of such admixtures can be estimated as 6 – 14%, based on the P1 and P2 widths. However, the Coulomb shift and width obtained with P3 are clearly not acceptable. Our overall feeling is that the cumulative information on ${}^6\text{He}$ and ${}^6\text{Be}$ g.s. is sufficient to choose P2 as the only acceptable potential.

IV. THEORETICAL DISCUSSION

As we have already mentioned, most of the attention in the studies of the $A=6$ isobar has been paid to ${}^6\text{He}$. Even in the studies of ${}^6\text{Be}$, there are only few works which studied its width. In addition, there has been only limited studies of the ${}^6\text{Be}$ g.s. decay correlations. The first consistent calculations of the ${}^6\text{Be}$ three-body decay width were performed in Ref. [32] using the integral formalism. In papers [14, 15], the quantum-mechanical formalism for two-proton radioactivity and Coulombic three-body decay studies was developed. In these papers, the integral formalism was criticized in application to the decays of systems with strong three-body Coulomb interactions and a more preferable way to calculate widths was proposed [see, Eq. 11]. The value $\Gamma = 90$ keV was obtained in Ref. [14] with the P1 potential ($K_{\text{max}} = 20$), which as we can see in Fig. 6, is reasonably well converged.

In our approach, the effects of antisymmetrization are taken into account in a simplified way. However, there are studies that treated the ${}^6\text{Be}$ decay as a 6-body problem. In RGM calculations [39], the ${}^6\text{Be}$ width of $\Gamma = 160$ keV for $E_{3r} = 1.52$ MeV was found using the complex scaling method. Scaling this value to the experimental $2p$ decay energy with the help of Fig. 5 we obtain $\Gamma = 125$ keV which is considerably larger than the experimental value. An interesting algebraic method was developed for studies of ${}^6\text{Be}$ decay in Ref. [40]. Here, the hyperspherical decomposition is used for the WF both in the internal

region (6-body HHs) and in the asymptotic region (three-body cluster HHs). A calculated width of $\Gamma = 72$ keV was obtained for $E_{3r} = 1.172$ MeV which scales to $\Gamma = 110$ keV at the experimental $2p$ decay energy. In addition, we can expect a 10 – 15% reduction due to the absence of the $S = 1$ component in these calculations. This component is important in the internal region, but does not contribute to the width significantly. In addition, we can also expect roughly a factor of 2 increase due to the small basis size ($K_{\text{max}} = 10$) used in the asymptotic region in Ref. [40]. According to Fig. 6, with $K_{\text{max}} = 10$ we can expect only 60% of the width, at most. It seems that Ref. [40] is more a concept demonstration, rather than a realistic calculation. Therefore at the present moment, it is not possible to draw any conclusions about importance of the 6-body effects in calculations of the ${}^6\text{Be}$ decay properties.

The width of the ${}^6\text{Be}$ g.s. was calculated in Ref. [38] via a method analogous to ours (hyperspherical harmonics), but having certain technical differences. An approximate treatment of the $3 \rightarrow 3$ scattering is introduced in this work and the width is extracted from the energy behavior of the phase shifts. The width obtained was $\Gamma = 65$ keV for $E_{3r} = 1.26$ MeV which scales to $\Gamma = 84$ keV at the experimental $2p$ decay energy. It can be found in Ref. [38] that the calculation does not seem converged. If we extrapolate from $\Gamma = 84$ keV using the convergence curves for P2, P3, then the value $\Gamma = 110$ keV is obtained, which is in a good agreement with our P2 result.

An important result of the present work is the clear demonstration that any approach purporting to give satisfactory description of the ${}^6\text{Be}$ g.s. decay properties should have a certain “dynamic range” both in radial and functional spaces (see Table III). It can be found that not all of these conditions are satisfied in these other works dedicated to ${}^6\text{Be}$.

Our calculations demonstrate a noticeable sensitivity of the observables in the decay of ${}^6\text{Be}$ g.s. to the ingredients of the model. Table II demonstrates that this sensitivity is enhanced in ${}^6\text{Be}$ compared to ${}^6\text{He}$. Typical variations of the observables for ${}^6\text{He}$ are 0.5 – 4%, while in ${}^6\text{Be}$ there is about a 60% difference in between the widths calculated with P1 and P3. The tunneling process can be seen as a kind of a “quantum amplifier”, which drastically emphasizes minor features in the structure. For that reason, it is possible that the indirect probe of ${}^6\text{Be}$ decay is a more sensitive tool for determining the halo properties of ${}^6\text{He}$ than direct investigations of ${}^6\text{He}$ itself. We are referring to precision measurements of the correlations in ${}^6\text{Be}$ decay which are discriminative with respect to the fine details of the momentum distributions. In the experimental studies presented in this work, the quality of the data is approaching fulfillment of such a high precision request.

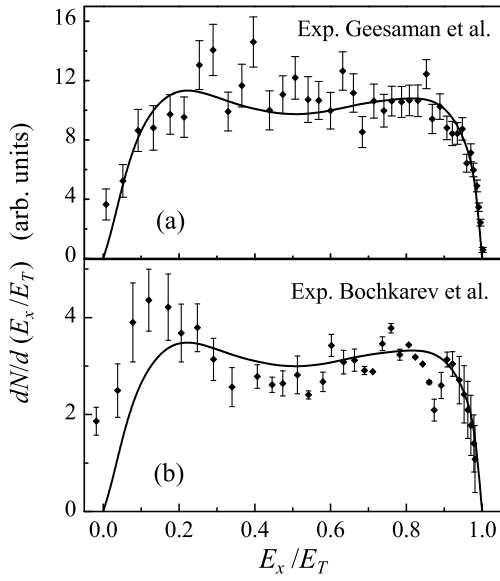


FIG. 14: Experimental energy distributions between protons in the decay of ${}^6\text{Be}$ measured in (a) Ref. [42] and (b) Ref. [30]. The theoretical prediction (P1) is provided only to guide the eye, as now we have no idea about the required experimental corrections.

V. EXISTING EXPERIMENTAL KNOWLEDGE ABOUT ${}^6\text{Be}$

Very precise results about the energy and width of the ${}^6\text{Be}$ g.s. were obtained in the early studies: $E_T = 1371(5)$ keV, $\Gamma = 89(6)$ keV [41]. The current value of the width is only slightly different $\Gamma = 92(6)$ keV [2].

The first measurements of ${}^6\text{Be}$ decay correlations were made in Ref. [42], see Fig. 14(a). They determined the energy spectrum of α -particles reconstructed in the ${}^6\text{Be}$ c.m. frame. For ${}^6\text{Be}$ g.s. events, this spectrum is the same as the correlation spectrum between two protons. The authors could not fit the data using simplistic decay scenarios (phase volume, diproton decay, simultaneous emission of p -wave protons) and concluded: “...no incoherent sum of the processes considered here will fit the data. Perhaps a full three-body computation is necessary to understand the energy spectrum.”

This ground-state decay, as well as decays of the 2^+ , $T = 0$ states of the $A=6$ isobar, was further investigated

TABLE III: Minimal dynamical ranges of calculations required to provide reasonably converged different observables for ${}^6\text{Be}$. Different basis sizes are required for simplistic BJ and realistic GPT potentials in the p - p channel.

value	E_{3r}	Γ	distributions
ρ_{\max} (fm)	20	60	300
K_{\max} (SBB+BJ)	16	30	80
K_{\max} (SBB+GPT)	40	70	110

in the series of works by the Kurchatov Institute group [28, 30, 31, and Refs. therein], see Fig. 14(b). They developed a method of analyzing the p - p correlations in the framework of a three-body partial-wave decomposition and applied this to the three-body decays of light nuclei [29, 30]. In particular, the first kinematically complete study of ${}^6\text{Be}$ proved the existence of three-particle $p+p+\alpha$ correlations with $S(p-p) = 1$ and $S(p-p) = 0$ [30, 31] which matched the three-body components found theoretically in the p -shell structure of ${}^6\text{Be}$ [26]. One of the important result for ${}^6\text{Be}$ g.s. was the realization that $S(p-p) = 0$ and $S(p-p) = 1$ components of the WF should produce very different correlation patterns. The presence of an “admixture” of $S(p-p) = 1$ component to the WF was demonstrated by an experiment performed with special kinematics. In these works, the concept of “democratic decay” was coined. This describes the specific decay mode for three-body systems, when the events are not highly focused in narrow kinematical regions, but are distributed broadly (“democracy” among different kinematical regions). “Democratic decay” is now a popular term for this class of phenomena, but the correlations in ${}^6\text{Be}$ decay have never been studied since that time. The spectra shown in Figs. 14 (a) and (b) are not in complete agreement with each other. Furthermore, there are large statistical uncertainties and the geometry of experiments may cause cuts in kinematical space which make comparison the theory difficult. It is clear a modern experiment on ${}^6\text{Be}$ decay was needed.

VI. EXPERIMENT

A. Experimental Method

The Texas A&M University K500 cyclotron facility was used to produce a 200 pA beam of ${}^{10}\text{B}$ at $E/A = 15.0$ MeV. This primary beam impinged on a hydrogen gas cell held at a pressure of 2 atmospheres and kept at liquid-nitrogen temperature. A secondary beam of $E/A = 10.7$ MeV ${}^{10}\text{C}$ was produced through the ${}^{10}\text{B}(p,n){}^{10}\text{C}$ reaction and separated from other reaction products using the MARS spectrometer [43]. This secondary beam, with intensity of $2 \times 10^5 \text{ s}^{-1}$, purity of 99.5%, an energy spread of 3%, and a spot size of 3.5×3.5 mm was inelastically excited due to interactions with 14.1 mg/cm^2 Be and 13.4 mg/cm^2 C targets. Ground-state ${}^6\text{Be}$ fragments were created from the α decay of these excited ${}^{10}\text{C}$ particles. Following the decay of the ${}^6\text{Be}$ g.s. fragment, the final exit channel is $2p+2\alpha$.

The four decay products were detected in an array of four Si E - ΔE telescopes located in a plane 14 cm downstream of the target. The telescopes, part of the HIRA array [44], consisted of a $65 \mu\text{m}$ thick, single-sided Si-strip ΔE detector followed by a 1.5 mm thick, double-sided Si strip E detector. All Si detectors were 6.4×6.4 cm in area with their position-sensitive faces divided into 32 strips. The telescopes were positioned in a square arrangement

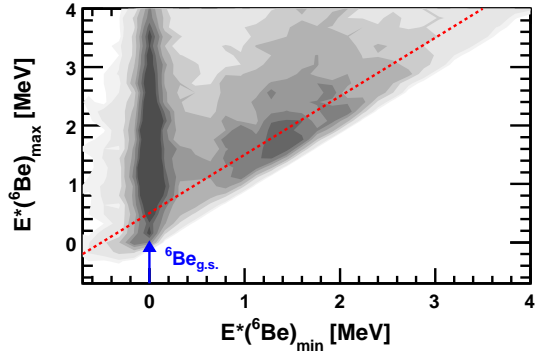


FIG. 15: Contour plot showing the distribution of the two possible ${}^6\text{Be}$ excitation energies that can be associated with the two $2p+\alpha$ subevents ordered by the maximum and minimum values. The dashed line indicates the threshold for which correct identification of the $2p+\alpha$ subevent associated with ${}^6\text{Be}$ decay is achieved in the simulations. The ridge associated with ${}^6\text{Be}$ g.s. decay is indicated by the arrow.

with each telescope offset from its neighbor to produce a small, central, square hole through which the unscattered beam passed. With this arrangement, the angular range from $\theta = 1.3$ to 7.7° was covered. More details of the experimental arrange can be found in Ref. [11].

B. Monte Carlo Simulations

Monte Carlo simulations of the experiment were performed in order to determine the experiment bias and to understand the effects of the gates applied to remove unwanted $2p+2\alpha$ events. The simulations included the α decay of the parent ${}^{10}\text{C}$ fragments and the correlations between the ${}^6\text{Be}$ decay products are sampled according to the theory of Sect. III B. The effects of energy loss and small-angle scattering of all the decay products were considered following Refs. [45, 46].

Simulated events were passed through a detector filter and the effects of the position and energy resolution of the detector were added. The “detected” simulated events were subsequently analyzed in the same manner as the experimental data. The velocity, excitation-energy, and angular distributions of the parent ${}^{10}\text{C}$ states were chosen such that the secondary distributions that passed the detector filter were consistent with the experimental results. Similar simulations for other decay modes were found to reproduce the experimental resolution [11].

C. Event Selection

Apart from α - ${}^6\text{Be}$ g.s. decay, there are many other ${}^{10}\text{C}$ decay modes that lead to the $2p+2\alpha$ exit channel and thus the detected events must be suitably gated to re-

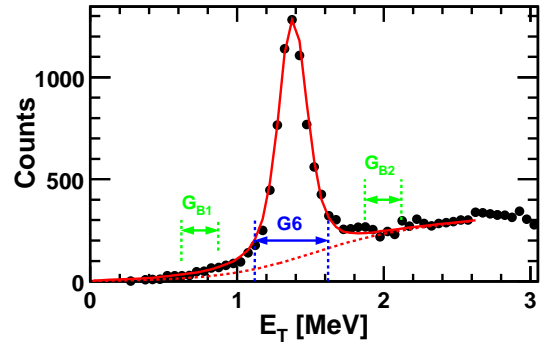


FIG. 16: (Color online) Experimental distribution of E_T for selected events is shown by the data points. The solid curve indicates the distribution predicted by the Monte Carlo simulation with the addition of a smooth background (dashed curve). The $G6$ gate used to select ${}^6\text{Be}$ g.s. events and the two gates (G_{B1} , G_{B2}), used to estimate the background under the peak, are indicated.

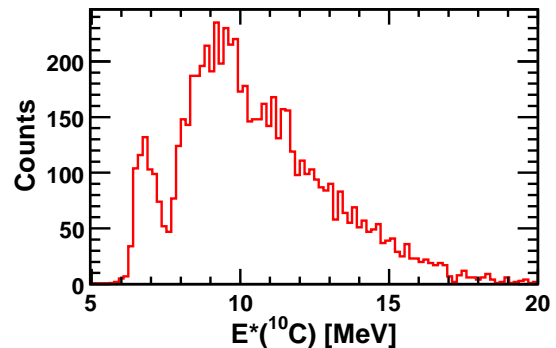


FIG. 17: (Color online) Experimental distribution of ${}^{10}\text{C}$ excitation energy for α - ${}^6\text{Be}$ events selected in this study.

move these unwanted decays. Of particular importance is the rejection of the large yield of decays where the ${}^{10}\text{C}$ fragments undergoes two-proton decay (either sequential through ${}^9\text{B}$ or prompt) leading to the creation of an ${}^8\text{Be}$ g.s. [11]. These events can readily be identified from the correlations between the two α particles. The distribution of relative energy ($E_{rel}^{\alpha\alpha}$) between the two α particles contains a strong, narrow peak corresponding to ${}^8\text{Be}$ g.s. decay [11]. This peak has a FWHM of 38 keV and sits on a negligible background [11] thus allowing for a clean rejection of these events with the gate $E_{rel}^{\alpha\alpha} < 0.2$ MeV. Our Monte Carlo simulations suggests this gate has essentially no significant effect on true α - ${}^6\text{Be}$ g.s. decays with only 0.01% of detected events being rejected.

The remaining events have contributions from α - ${}^6\text{Be}$ g.s. and p - ${}^9\text{B}$ ($E^*=2.43$ MeV) decays [11]. The latter ${}^9\text{B}$ excited state does not decay through ${}^8\text{Be}$ g.s. but undergoes a three-body decay like the ${}^6\text{Be}$ ground state. For

both of these decays modes, there is a difficulty in trying to find the intermediate state (either ${}^6\text{Be}$ or ${}^9\text{B}$) as there are two possible ways to construct this fragment from the detected $2p+2\alpha$ exit channel. Let us concentrate on the ${}^6\text{Be}$ g.s. fragments first where we must determine which of the two detected α particles was the one initially emitted from the ${}^{10}\text{C}$ parent and which was produced in the decay of ${}^6\text{Be}$. To this end, the ${}^6\text{Be}$ excitation energy for the two ways of constructing the ${}^6\text{Be}$ fragment are determined and ordered according to their maximum and minimum values; $E^*({}^6\text{Be})_{\text{max}}$ and $E^*({}^6\text{Be})_{\text{min}}$. A two dimensional plot of these two excitation energies is shown in Fig. 15. A prominent ridge centered around $E^*({}^6\text{Be})_{\text{min}} = 0$ corresponding to ${}^6\text{Be}$ g.s. decay is clearly visible. For those events in this ridge structure, the identification of which α particles was produced in ${}^6\text{Be}$ decay is clearly the one associated with $E^*({}^6\text{Be})_{\text{min}}$ when $E^*({}^6\text{Be})_{\text{max}} \gg E^*({}^6\text{Be})_{\text{min}}$. However when $E^*({}^6\text{Be})_{\text{max}} \sim E^*({}^6\text{Be})_{\text{min}}$ the Monte Carlo simulations indicate that misidentifications will occur. These simulations suggest that for $E^*({}^6\text{Be})_{\text{max}} - E^*({}^6\text{Be})_{\text{min}} = 0.5$ MeV, the probability of misidentifying the α particles is 0.03%. This condition is indicated in Fig. 15 by the dashed line and only events above this line were used in the subsequent analysis of the experimental data. One can see from Fig. 15 that this condition does not significantly cut into the ridge structure and the Monte Carlo simulations suggest we lose 4.7% of the remaining α - ${}^6\text{Be}$ g.s. events with this gate.

The remaining ridge structure still sits on a background. Part of this background can be traced to ${}^{10}\text{C} \rightarrow p+{}^9\text{B}$ ($E^* = 2.43$ MeV) decays. These events can be identified from $E^*({}^9\text{B})_{\text{max}}$ and $E^*({}^9\text{B})_{\text{min}}$ information in a manner similar to the α - ${}^6\text{Be}$ g.s. events. A ridge structure also is evident in this case and it also sits on a non-negligible background, which in turn has contributions from α - ${}^6\text{Be}$ g.s. decay. Although one cannot completely separate all p - ${}^9\text{B}$ and α - ${}^6\text{Be}$ events, we do reject events in the $E^*({}^9\text{B})_{\text{min}}$ ridge structure. This results in a slightly diminished yield of true α - ${}^6\text{Be}$ g.s. events, but more importantly, it reduces the relative background under the ${}^6\text{Be}$ ridge structure shown in Fig. 15. The Monte Carlo simulations suggest only 2.7% of the remaining true α - ${}^6\text{Be}$ g.s. events were rejected by this condition.

The distribution of E_T for the final selection of events is shown in Fig. 16 by the data points. The FWHM width of the peak associated with ${}^6\text{Be}$ g.s. is 220 keV which is larger than the intrinsic value of $\Gamma = 92$ keV due to detector resolution. The solid curve indicates the simulated distribution after a smooth background contribution (dashed curve) is added. This simulated distribution reproduces the experimental results quite well confirming that the Monte Carlo simulations correctly model the experimental resolution. Figure 16 also shows the gate $G6$ used to select ${}^6\text{Be}$ g.s. fragments and the two gates, G_{B1} and G_{B2} which, when combined, were used to estimate the background in the $G6$ gate. In all subsequent results, this background has been subtracted.

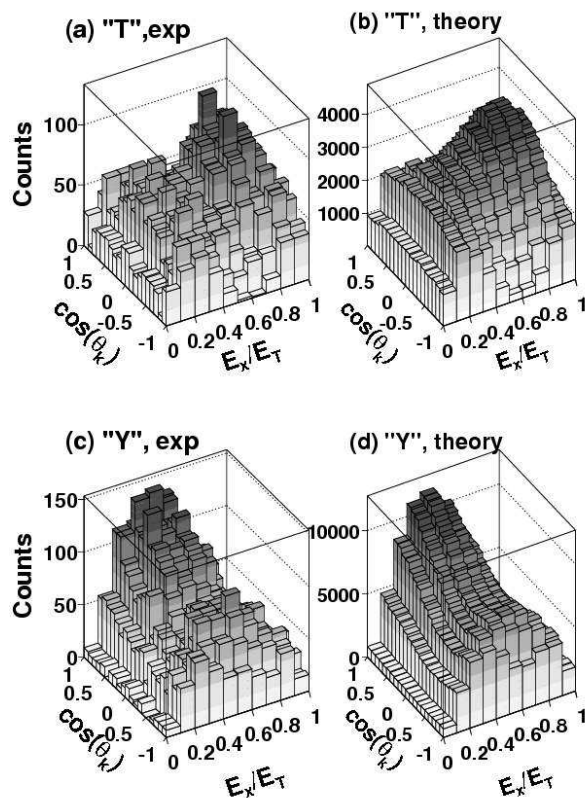


FIG. 18: Comparison of (a,c) experimental (exp) and (b,d) theoretical correlations for ${}^6\text{Be}$ g.s. decay presented in both the (a,b) “T” and (c,d) “Y” Jacobi systems. The theoretical distributions include the effects of the detector bias and resolution.

The excitation-energy distribution of ${}^{10}\text{C}$ fragments associated with the selected events is shown in Fig. 17. There is localized strength around $E^*({}^{10}\text{C}) = 7$ MeV and a continuous distribution up to approximately 15 MeV. Thus many ${}^{10}\text{C}$ excited states are contributing to the detected ${}^6\text{Be}$ g.s. yield.

VII. COMPARISON OF THEORY AND EXPERIMENT

Comparisons of experimental and predicted correlations in both the “T” and “Y” Jacobi systems are shown in Fig. 18. The experimental results [Figs. 18(a) and 18(c)] has been background subtracted and, for the predicted distributions [Figs. 18(b) and 18(d)], the effects of the detector resolution and bias has been incorporated via the Monte Carlo simulations. In this and subsequent plots, the simulated results has been normalized to the same number of counts as for the experiment data. In determining the Jacobi coordinates, there are two ways of choosing the order of the proton. For the experimental events, Jacobi coordinates were determined for both of these ways and thus each event contributes two counts

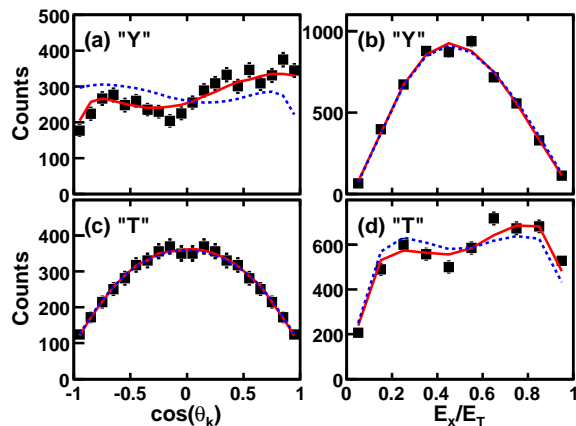


FIG. 19: (Color online) Comparison of the experimental (data points) and predicted (curves) distributions of E_x/E_T in the “T” (c), (d) and “Y” (a), (b) Jacobi systems. The blue dashed curves show the primary predicted distributions while the red solid curves include the effect of the detector bias and resolution. The theoretical results were obtained with the P2 potential.

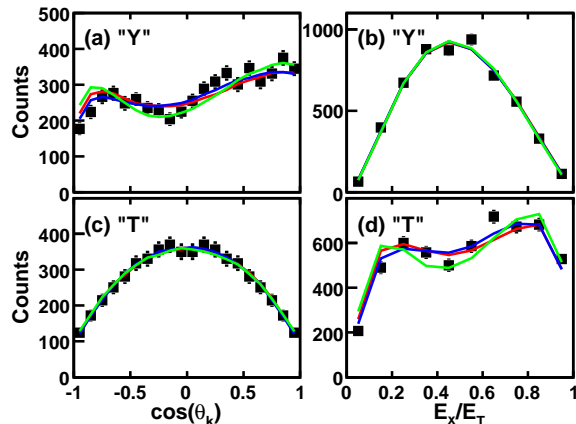


FIG. 20: (Color online) Comparison of the experimental (data points) and different predicted (curves) distributions of E_x/E_T in the “T” (c), (d) and “Y” (a), (b) Jacobi systems. The red, blue, and green curves correspond to P1, P2, and P3 potential sets respectively. The effect of the detector bias and resolution is included for the theoretical curves.

to the spectra. For “T” system, this forces the $\cos(\theta_k)$ distribution to be symmetrized around $\cos(\theta_k)=0$. General overall agreement between theory and experiment is found, although statistical fluctuations are the limiting factor for the experimental data.

To allow for a more detailed comparison, we compare projections of the correlations on both the E_x/E_T and $\cos(\theta_k)$ axes in Fig 19. The experimental data are indicated by the data points while the dashed and solid curves show the predictions before and after the simulated bias of the experimental apparatus is included. Interestingly, the “soft” observables (energy distribution

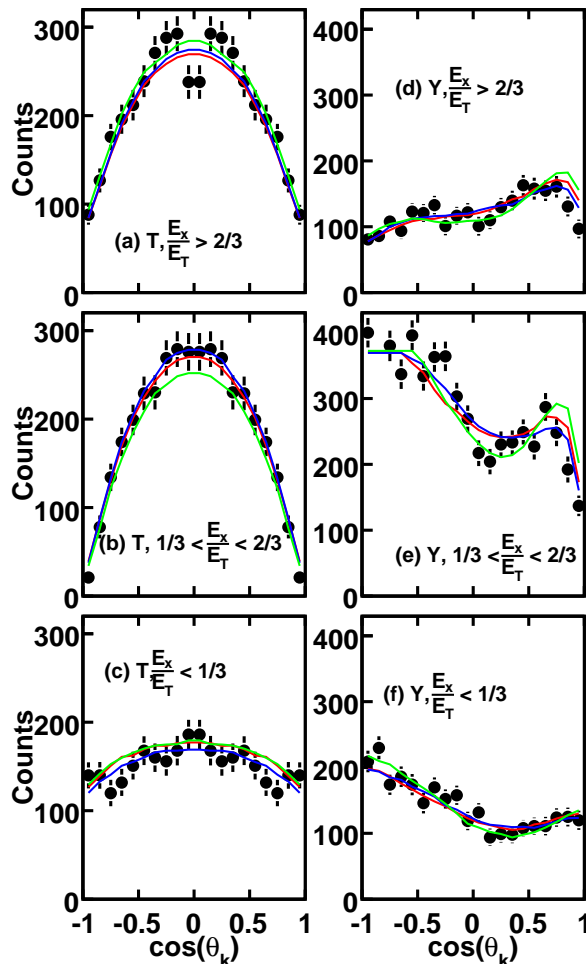


FIG. 21: (Color online) Comparison of experimental (data points) and predicted (curves) $\cos(\theta_k)$ distributions in the “T” (left) and “Y” (right) Jacobi systems for the indicated gates on E_x/E_T parameter. The red, blue, and green curves correspond to P1, P2, and P3 potential sets respectively. The effect of the detector bias and resolution is included.

in the “T” system and the angular distribution in the “Y” system) which have the most sensitivity to the ingredients of the theoretical calculations and its numerical implementation also have the largest bias induced by the detector apparatus. The other projected distributions (angular distribution in “T” and energy distribution in “Y”) are practically unaffected the detector response.

The same comparison of theory and data for all three potentials P1-P3 is shown in Fig. 20. All three sets of predictions reproduce the experimental data reasonable well. To highlight more details of the correlations, we show the $\cos(\theta_k)$ distributions gated on three equal region of E_x/E_T in Fig. 21 for the “T” and “Y” Jacobi systems. Reasonable agreement between the experiment (data points) and the three calculations (curves) is also found, although the P1 and P2 calculation are somewhat better. To quantify this, we determine the χ^2 per de-

TABLE IV: χ^2 per degree of freedom for fits to the complete correlations data in the “T” and “Y” system with the three assumed potentials

potential	“T”	“Y”
P1	1.29	1.25
P2	1.17	1.14
P3	1.58	1.45

gree of freedom (χ^2/ν) of the theoretical fit to the two-dimension data of Fig. 18. These values are listed in Table IV for both the “T” and “Y” systems. For a good fit were need $\chi^2/\nu \sim 1$ and clearly both P1 and P2 satisfy this criteria. Again we find the P3 calculation is somewhat worse.

VIII. CONCLUSIONS

The first detailed studies of the correlations from the decay of ${}^6\text{Be}$ g.s. are performed both experimentally and theoretically. We have found that certain correlations (namely, energy correlation between two protons and angular correlations in “Y” Jacobi system) are quite sensitive to the details of structure and interactions. We demonstrated that relative sensitivity of correlation pat-

terns to the details of the interactions is higher in the decay of ${}^6\text{Be}$ compared to the corresponding sensitivity of typical observables in ${}^6\text{He}$. We argue that further highly detailed studies of correlations in the decay of ${}^6\text{Be}$ could provide a better access to the properties of $A=6$ isobar (and thus to halo properties of ${}^6\text{He}$ nucleus) than the direct studies of ${}^6\text{He}$ halo properties.

Experimentally ${}^6\text{Be}$ fragments are produced from the α decay of ${}^{10}\text{C}$ excited states formed by inelastically scattering a ${}^{10}\text{C}$ beam off of Be and C targets. The $\alpha+2p$ decay products as well as the initially emitted α particle were detected in a Si array with good position and energy resolution. The experimentally measured correlations between ${}^6\text{Be}$ g.s. decay products and the theoretical predicts were found to be in good agreement.

IX. ACKNOWLEDGEMENTS

This work was supported by the U.S. Department of Energy, Division of Nuclear Physics under grants DE-FG02-87ER-40316, DE-FG02-93ER40773, and DE-FG02-04ER413. L.V.G. acknowledge the support from Russian Foundation for Basic Research grants RFBR 08-02-00892, RFBR 08-02-00089-a, and Russian Ministry of Industry and Science grant NS-3004.2008.2.

-
- [1] V.I. Goldansky, Nucl. Phys. **19**, 482 (1960).
[2] D. R. Tilley, C. M. Cheves, J. L. Godwina, G. M. Haled, H. M. Hofmann, J. H. Kelley, C. G. Sheua, H. R. Weller, Nucl. Phys. **A708**, 3 (2002).
[3] M. Pfutzner, E. Badura, C. Bingham, B. Blank, M. Chartier, H. Geissel, J. Giovinazzo, L. V. Grigorenko, R. Grzywacz, M. Hellstrom, Z. Janas, J. Kurcewicz, A. S. Lalleman, C. Mazzocchi, I. Mukha, G. Munzenberg, C. Plettner, E. Roeckl, K. P. Rykaczewski, K. Schmidt, R. S. Simon, M. Stanoiu, J.-C. Thomas, Eur. Phys. J. **A14**, 279 (2002).
[4] J. Giovinazzo, B. Blank, M. Chartier, S. Czajkowski, A. Fleury, M. J. Lopez Jimenez, M. S. Pravikoff, J.-C. Thomas, F. de Oliveira Santos, M. Lewitowicz, V. Maslov, M. Stanoiu, R. Grzywacz, M. Pfutzner, C. Borcea, B. A. Brown, Phys. Rev. Lett. **89**, 102501 (2002).
[5] C. Dossat, A. Bey, B. Blank, G. Canchel, A. Fleury, J. Giovinazzo, I. Matea, F. de Oliveira Santos, G. Georgiev, S. Grèvy, I. Stefan, J. C. Thomas, N. Adimi, C. Borcea, D. Cortina Gil, M. Caamano, M. Stanoiu, F. Aksouh, B. A. Brown, and L. V. Grigorenko, Phys. Rev. C **72**, 054315 (2005).
[6] B. Blank, A. Bey, G. Canchel, C. Dossat, A. Fleury, J. Giovinazzo, I. Matea, N. Adimi, F. De Oliveira, I. Stefan, G. Georgiev, S. Grevy, J. C. Thomas, C. Borcea, D. Cortina, M. Caamano, M. Stanoiu, F. Aksouh, B. A. Brown, F. C. Barker, and W. A. Richter, Phys. Rev. Lett. **94**, 232501 (2005).
[7] J. Giovinazzo, B. Blank, C. Borcea, G. Canchel, J.-C. Dalouzy, C. E. Demonchy, F. de Oliveira Santos, C. Dossat, S. Grevy, L. Hay, J. Huikari, S. Leblanc, I. Matea, J.-L. Pedroza, L. Perrot, J. Pibernat, L. Serani, C. Stodel, J.-C. Thomas, Phys. Rev. Lett. **99**, 102501 (2007).
[8] K. Miernik, W. Dominik, Z. Janas, M. Pfützner, L. Grigorenko, C. R. Bingham, H. Czyrkowski, M. Cwiok, I. G. Darby, R. Dabrowski, T. Ginter, R. Grzywacz, M. Karny, A. Korgul, W. Kusmierz, S. N. Liddick, M. Rajabali, K. Rykaczewski, and A. Stolz, Phys. Rev. Lett. **99**, 192501 (2007).
[9] I. Mukha, K. Sümmerer, L. Acosta, M. A. G. Alvarez, E. Casarejos, A. Chatillon, D. Cortina-Gil, J. Espino, A. Fomichev, J. E. García-Ramos, H. Geissel, J. Gómez-Camacho, L. Grigorenko, J. Hofmann, O. Kiselev, A. Korshennikov, N. Kurz, Yu. Litvinov, I. Martel, C. Nociforo, W. Ott, M. Pfutzner, C. Rodríguez-Tajes, E. Roeckl, M. Stanoiu, H. Weick, and P. J. Woods, Phys. Rev. Lett. **99**, 182501 (2007).
[10] I. Mukha, L. Grigorenko, K. Sümmerer, L. Acosta, M. A. G. Alvarez, E. Casarejos, A. Chatillon, D. Cortina-Gil, J. M. Espino, A. Fomichev, J. E. Garcia-Ramos, H. Geissel, J. Gomez-Camacho, J. Hofmann, O. Kiselev, A. Korshennikov, N. Kurz, Yu. Litvinov, I. Martel, C. Nociforo, W. Ott, M. Pfützner, C. Rodriguez-Tajes, E. Roeckl, M. Stanoiu, H. Weick, and P. J. Woods, Phys. Rev. C **77**, 061303(R) (2008).
[11] K. Mercurio, R. J. Charity, R. Shane, L. G. Sobotka, J. M. Elson, M. Famiano, A. H. Wuosmaa, A. Banu, C. Fu, L. Trache, R. E. Tribble, A. M. Mukhamedzhanov, Phys.

- Rev. C **78**, 031602 (2008).
- [12] I. Mukha, E. Roeckl, L. Batist, A. Blazhev, J. Döring, H. Grawe, L. Grigorenko, M. Huyse, Z. Janas, R. Kirchner, M. La Commara, C. Mazzocchi, S. L. Tabor, P. Van Duppen, *Nature* **439**, 298 (2006).
- [13] O. L. Pechenaya, C. J. Chiara, D. G. Sarantites, W. Reviol, R. J. Charity, M. P. Carpenter, R. V. F. Janssens, T. Lauritsen, C. J. Lister, D. Seweryniak, S. Zhu, L.-L. Andersson, E. K. Johansson, and D. Rudolph, *Phys. Rev. C* **76**, 011304 (2007).
- [14] L. V. Grigorenko, R. C. Johnson, I. G. Mukha, I. J. Thompson, and M. V. Zhukov, *Phys. Rev. Lett.* **85**, 22 (2000).
- [15] L. V. Grigorenko, R. C. Johnson, I. G. Mukha, I. J. Thompson, and M. V. Zhukov, *Phys. Rev. C* **64**, 054002 (2001).
- [16] L. V. Grigorenko and M. V. Zhukov, *Phys. Rev. C* **68**, 054005 (2003).
- [17] L. V. Grigorenko, I. G. Mukha, I. J. Thompson, and M. V. Zhukov, *Phys. Rev. Lett.* **88**, 042502 (2002).
- [18] L. V. Grigorenko, R. C. Johnson, I. G. Mukha, I. J. Thompson, and M. V. Zhukov, *Eur. Phys. J. A* **15** 125 (2002).
- [19] L. V. Grigorenko, I. G. Mukha, and M. V. Zhukov, *Nucl. Phys.* **A713**, 372 (2003); erratum **A740**, 401 (2004).
- [20] L. V. Grigorenko, I. G. Mukha, and M. V. Zhukov, *Nucl. Phys.* **A714**, 425 (2003).
- [21] L. V. Grigorenko and M. V. Zhukov, *Phys. Rev. C* **76**, 014008 (2007).
- [22] L. V. Grigorenko and M. V. Zhukov, *Phys. Rev. C* **76**, 014009 (2007).
- [23] S. Sack, L. C. Biedenharn, G. Breit, *Phys. Rev.* **93**, 321 (1954).
- [24] G. E. Brown and A. D. Jackson, *The nucleon-nucleon interaction*, North Holland Publishing Company, Amsterdam/Oxford, 1976.
- [25] D. Gogny, P. Pires, R. de Tourreil, *Phys. Lett.* **B32**, 591 (1970).
- [26] B.V. Danilin, M. V. Zhukov, S. N. Ershov, F. A. Gareev, R. S. Kurmanov, J. S. Vaagen, and J. M. Bang, *Phys. Rev. C* **43**, 2835 (1991).
- [27] M. S. Golovkov, L. V. Grigorenko, A. S. Fomichev, Yu. Ts. Oganessian, Yu. I. Orlov, A. M. Rodin, S. I. Sidorchuk, R. S. Slepnev, S. V. Stepantsov, G. M. Ter-Akopian, R. Wolski, *Phys. Lett.* **B588**, 163 (2004).
- [28] O. V. Bochkarev, A. A. Korsheninnikov, E. A. Kuz'min, I. G. Mukha, A. A. Ogloblin, L. V. Chulkov, G. B. Yan'kov, *Yad. Fiz.* **46** 12 (1987).
- [29] B. V. Danilin, M. V. Zhukov, A. A. Korsheninnikov, L. V. Chulkov, V. D. Efros, *Yad. Fiz.* **46**, 427 (1987) [*Sov. J. Nucl. Phys.* **46**, 225 (1987)].
- [30] O. V. Bochkarev, L. V. Chulkov, A. A. Korsheninnikov, E. A. Kuzmin, I. G. Mukha, G. B. Yankov, *Nucl. Phys.* **A505**, 215 (1989).
- [31] O. V. Bochkarev, A. A. Korsheninnikov, E. A. Kuz'min, I. G. Mukha, L. V. Chulkov, G. B. Yan'kov, *Yad. Fiz.* **55**, 1729 (1992) [*Sov. J. Nucl. Phys.* **55**, 955 (1992)].
- [32] B. V. Danilin and M. V. Zhukov, *Yad. Fiz.* **56**, 67 (1993) [*Phys. At. Nucl.* **56**, 460 (1993)].
- [33] L.-B. Wang, P. Mueller, K. Bailey, G. W. F. Drake, J. P. Greene, D. Henderson, R. J. Holt, R. V. F. Janssens, C. L. Jiang, Z.-T. Lu, T. P. O'Connor, R.C.Pardo, K. E. Rehm, J. P. Schiffer, X. D. Tang, *Phys. Rev. Lett.* **93**, 142501 (2004).
- [34] P. Mueller, I. A. Sulai, A. C. C. Villari, J. A. Alcantara-Nunez, R. Alves-Conde, K. Bailey, G. W. F. Drake, M. Dubois, C. Eleon, G. Gaubert, R. J. Holt, R. V. F. Janssens, N. Lemesne, Z.-T. Lu, T. P. O'Connor, M.-G. Saint-Laurent, J.-C. Thomas, L.-B. Wang, *Phys. Rev. Lett.* **99**, 252501 (2007).
- [35] P. Egelhof, *Prog. Part. Nucl. Phys.* **46**, 307 (2001).
- [36] A. Ozawa, T. Suzuki, I. Tanihata, *Nucl. Phys.* **A693**, 32 (2001).
- [37] G. A. Miller, *Phys. Rev. Lett.* **99**, 112001 (2007).
- [38] P. Descouvemont, E. Tursunov, D. Baye, *Nucl. Phys.* **A765**, 370 (2006).
- [39] A. Csoto, *Phys. Rev. C* **49**, 3035 (1994).
- [40] V. Vasilevsky, A. V. Nesterov, F. Arickx, and J. Broeckhove, *Phys. Rev. C* **63**, 034607 (2001).
- [41] W. Whaling, *Phys. Rev. C*, **150**, 836 (1966).
- [42] D. F. Geesaman, R. L. McGrath, P. M. S. Lesser, P. P. Urone, B. VerWest, *Phys. Rev. C* **15**, 1835 (1977).
- [43] R. E. Tribble, R. H. Burch, and C. A. Gagliardi, *Nucl. Instrum. Meth.* **A285**, 411 (1989).
- [44] M. S. Wallace, M. A. Famiano, M.-J. van Goethem, A. M. Rogers, W. G. Lynch, J. Clifford, F. Delaunay, J. Lee, S. Labostov, M. Mocko, L. Morris, A. Moroni, B. E. Nett, D. J. Oostdyk, R. Krishnasamy, M. B. Tsanga, R. T. de Souza, S. Hudan, L. G. Sobotkad, R. J. Charity, J. Elsond, and G. L. Engel, *Nucl. Instrum. Meth.* **A583**, 302 (2007).
- [45] J. F. Ziegler, J. P. Biersack, and U. Littmark, *The Stopping and Range of Ions in Solids*, Pergamon Press, New York, (1985). The code SRIM can be found at <http://www.srim.org>.
- [46] R. Anne, J. Herault, R. Bimbot, H. Gauvin, G. Bastin, and F. Hubert, *Nucl. Instrum. Meth.* **B34**, 295 (1988).
- [47] Evident exception is, of cause, the β -decay of ${}^6\text{He}$ and β -delayed particle emission. These reactions exploit very "reliable" weak probe, providing important, but naturally limited information about this system.
- [48] There are, however, some very special situations which we can not discuss in this work.

TABLE V: Weights N_i of the dominating components of the ${}^6\text{He}$ and ${}^6\text{Be}$ g.s. WFs and the partial widths of the ${}^6\text{Be}$ g.s. WF in percent. The results are for the Jacobi “T” system. The normalizations of the ${}^6\text{Be}$ components are found for integration radius $\rho_{\text{int}} = 12.5$ fm.

i	Quantum numbers					$N_i({}^6\text{He})$			$N_i({}^6\text{Be})$			$\Gamma_i({}^6\text{Be})$		
	K	L	S	l_x	l_y	P1	P2	P3	P1	P2	P3	P1	P2	P3
1	0	0	0	0	0	4.32	4.65	4.27	6.72	7.24	6.65	50.44	50.77	41.03
2	2	0	0	0	0	78.36	80.73	79.40	75.71	77.49	75.28	33.48	33.74	41.52
3	2	1	1	1	1	14.19	11.28	12.02	13.09	10.60	11.44	3.89	3.31	6.15
4	4	0	0	0	0	0.03	0.04	0.02	0.10	0.14	0.07	2.03	2.11	2.25
5	4	0	0	2	2	0.48	0.50	0.58	0.44	0.45	0.53	6.10	6.48	4.97
6	6	0	0	0	0	0.01	0.02	0.01	0.02	0.03	0.01	1.63	1.26	1.49
7	6	0	0	2	2	1.13	1.18	1.56	1.56	1.60	2.32	0.67	0.73	0.78
8	6	1	1	3	3	0.57	0.54	0.75	0.79	0.75	1.18	0.08	0.06	0.09
9	8	0	0	0	0	0.28	0.31	0.37	0.47	0.51	0.66	0.85	0.69	0.85
10	8	0	0	2	2	0.17	0.17	0.25	0.28	0.28	0.46	0.08	0.11	0.10
11	8	0	0	4	4	0.03	0.03	0.04	0.05	0.05	0.08	0.37	0.40	0.32